PREDICTION OF ALL RIB DEFLECTIONS OF THOR-ATD BY MEANS OF DEEP NEURAL NETWORK MODEL

Takayuki Kawabuchi
Yasuhiro Dokko
Honda R&D Co., Ltd.
Japan

Hidenori Mikami
Honda Motor Co., Ltd
Japan

Kota Katsushima
IDAJ Co., LTD.
Japan

Yosuke Nagai
Photron Limited
Japan

Paper Number 23-0219

ABSTRACT

The fatality rate of thoracic injury for elderly occupants in vehicle accidents is significantly high. Its major cause is the rise of internal organ injury rates due to an increase in the number of fractured ribs (NFR). Therefore, NFR reduction is crucial to enhance elderly occupant protection and is one of the key issues for achieving zero fatalities. In order to improve NFR prediction accuracy, the previous study proposed the criterion using the weighted averaged displacement of all ribs (WADAR), which indicated a higher correlation coefficient with NFR than that of the criterion, Rmax, using four Infra-Red Telescoping Rod for the Assessment of Chest Compression (IR-TRACC) installed on the thorax of the Test device for Human Occupant Restraint Anthropometric Test Dummy (THOR-ATD). While WADAR requires all rib deflections, it is difficult to install IR-TRACCs on all ribs inside the limited space in the thorax of THOR-ATD. The objective of this research is to predict the deflections of all ribs by means of a neural network model using time-histories of rib deflections from four IR-TRACCs and the crash velocity without any installation of additional measurement devices.

The architecture of the neural network model is based on U-Net, which is one of the convolutional neural network models. The model was trained by time-historical X, Y and Z displacements of 14 ribs and the crash velocity derived from the 56 FEM simulation data, which represented frontal and oblique sled experiments with THOR-ATD. The model learned the physical relationships among the ribs with and without IR-TRACCs. The predicted rib deflections were validated by the THOR-ATD experiment, where the displacements of the 2nd to 6th ribs on the left side were measured three-dimensionally by the set of two cameras installed on the upper and lower thoracic spines.

The predicted deflections during 0 to 150 ms were processed into a resultant deflection and compared to the actual deflection through the 2nd to 6th ribs on the left side. The maximum differences in the peak deflection were 2.3 mm, respectively. Furthermore, the root mean square error (RMSE) was calculated at each rib for prediction accuracy evaluation, which resulted in minimum and maximum RMSE of 0.6 mm and 2.7 mm, respectively.

Although the number of training datasets was small, the neural network model trained by FEM simulation data could predict all the rib deflections with small error without physical measurement devices.

INTRODUCTION

Fatal thoracic injuries in frontal crashes appeared with frequency equal to, or following, head fatal injuries [1]. Kent et al. reported that the percentages of drivers who died with injuries related to rib fractures increased with aging and

suggested that rib fracture was associated with the significantly increasing fatality rate of thoracic injuries, especially in elderly occupants [2]. It is estimated that the population of adults over 65 years old will increase up to 83.7 million by the year 2050 in the United States [3] and it will result in an increasing number of drivers sustaining severe injury to the thorax in traffic accidents.

Since the number of fractured ribs (NFR) is correlated with a rise in a fatality rates of the elderly population [4][5][6], the criteria predicting NFR with high accuracy are necessary for the development of an occupant protection device.

Kent et al. suggested that the risk of rib fractures increased with the level of thoracic compression and the thoracic injury risk was often described by the antero-posterior deflection of the thorax [7]. The thoracic deflection is measured by sensors installed in the thorax of the Test device for Human Occupant Restraint Anthropometric Test Dummy (THOR-ATD). THOR-ATD has four Infra-Red Telescoping Rods for the Assessment of Chest Compression (IR-TRACC) and they are often used to estimate the injury level by criteria such as Rmax [8], which uses maximum resultant deflection, and PCscore [9] which is calculated by the formula based on the primary component analysis by means of four IR-TRACCs values.

Kawabuchi et al. reported that NFR increased without deformation at the ribs with IR-TRACCs when a region remote from those ribs, such as the clavicle or upper part of the rib cage, were impacted. Under such conditions, the criteria using weighted averaged displacement of all ribs (WADAR) correlated better with NFR than that of the other criteria such as Rmax [10]. Whereas WADAR requires all rib deflections, it is difficult to install IR-TRACCs on all ribs inside the limited space in the thorax of THOR-ATD. Hence, this study suggests a predictive solution instead of physical measurement devices.

Recent studies have investigated the application of physical simulation results to deep learning. Guo et al. developed the Deep Neural Network (DNN) model, which predicted a steady flow field by means of the latent fluid characteristics learned from computational fluid dynamics simulation results [11]. Ito et al. constructed a model that predicted pedestrian injury values by means of pedestrian crash simulation results [12]. As indicated in the previous studies, a DNN could learn a physical relationship between multiple outputs such as trajectories from the simulation results. For example, when the simulation well reconstructs the actual physical environment, the model trained by the simulation data predicts movement of one location in the actual experiment results from another separated location based on the latent physical relationship.

In order to construct such a DNN model, the following are prerequisites. First, the multiple outputs of the simulation results mutually interact based on common physical relationships. Second, the simulation well models the actual physical environment. Since 14 thoracic ribs of THOR-ATD are connected by a rubber bib, the all ribs move together with the four ribs equipped with IR-TRACC based on the physical characteristics. That is, all rib deflections may be predictable from the time-historical deflection data measured by four IR-TRACCs. Also, the specific mechanical properties applied in the finite elemental (FE) model of THOR-ATD were validated by the calibration test results. As above, since the simulation data used in this study conformed to the two prerequisites, it may enable the DNN model to learn the latent physical relationships between the movement of the ribs with and without IR-TRACCs from the FE simulation results. Moreover, the model may predict all rib deflections in physical THOR-ATD from waveforms measured by IR-TRACCs.

The objective of this study is to develop a DNN model learning latent mechanical properties from THOR-ATD simulation data and to predict the time-historical deflections of all ribs by means of four IR-TRACC deflection data.

METHOD

Structure of THOR-ATD

Figure 1 shows the structure of the thoracic part of THOR-ATD. The thoracic part represents the chest of a human body and consists of a sternum and 14 ribs, which are fewer than the 24 ribs of an actual rib cage. The ribs and the sternum are connected by the costal cartilage, which is represented by the part called the bib in THOR-ATD. The tip

of each rib is bolted onto the bib, and they are connected with the sternum plate. The sternum plate is divided into upper and lower parts, which are connected with the clavicle and 2nd to 7th ribs through the bib, respectively.

The IR-TRACCs consist of expandable tubes installed on the spine box and they are bolted on the respective tips of the 3rd and 6th ribs. An infrared ray is emitted in the tube and measures the change in rib deflections. The base of IR-TRACC on the spine box has Y and Z rotation axes with angle meters which make the tube move three-dimensionally. The spine box consists of upper and lower parts which are connected by the rubber block reproducing the bending movement of an actual spine. The 1st to 4th and 5th to 7th ribs are deformable steel plate with rubber damping materials and they are bolted onto the upper and lower spine boxes, respectively.

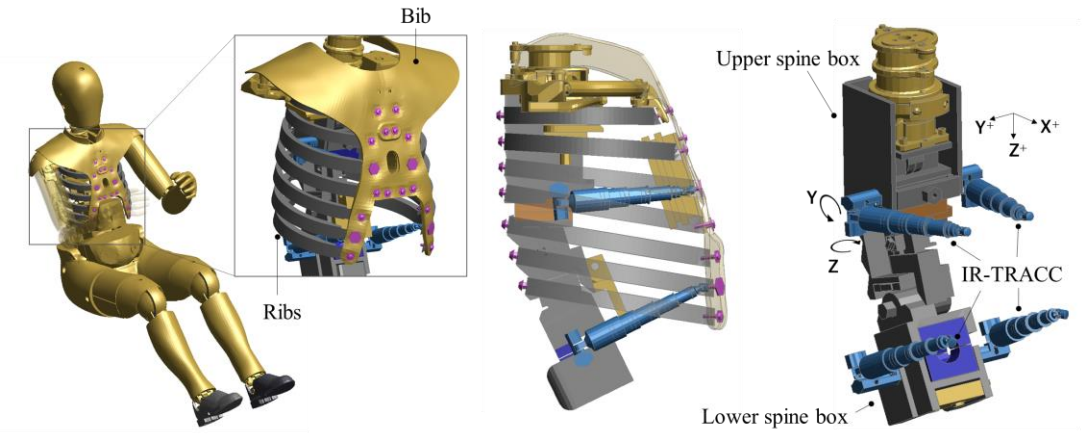

Figure 1. Illustration of the thoracic structure of THOR-ATD

Boundary Condition of FE Simulation for Training Data

The results of FE simulation (LS-DYNA R9.1.2) were utilized for the training data in this study. Figure 2 shows the boundary condition of the simulation, which reconstructs the frontal crash sled experiment conducted in European research project (SENIORS) [13]. The test rig had a steel pan for a seat, a seat belt, foot rests and a generic airbag by means of THOR-ATD FE model version 1.3.2 [14]. The table A1 shows the load cases with the test parameters: impact speed, impact angle and with/without airbags. The 150 ms time-historical X, Y and Z deflections of rib tips and the crash velocity were extracted from the 56 simulation results as training data.

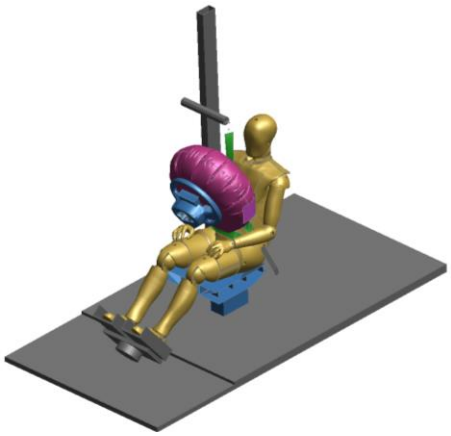

Figure 2. Illustration of the test rig

Deep Neural Network Model

The DNN model was constructed using the sled velocity and the X, Y and Z time-historical rib deflections of four ribs (13 waveforms) that can be measured experimentally by IR-TRACCs, which outputted the X, Y and Z time-historical rib deflections of 14 ribs (42 waveforms), including the four rib deflections that can be measured. The sled

velocity was considered to contain physical characteristics of crash modes and indirectly associated with thoracic deformation patterns. Figure 3 shows the processing concept of the model.

U-Net [15] was used for the architecture of the DNN in this study, which was suitable for segmentation and style transformation and is often used in image processing. Figure 4 shows the conceptual diagram of the U-Net structure used in this study. U-Net that is based on Autoencoder with skip-connections enables reconstruction of images or waveforms more accurately than those by Autoencoder. Skip-connections transfer local information conventionally lost in the encoding process to the decoding process, improving prediction accuracy. In this study, U-net was assumed to be suitable because the required task was to transform the style from a known to an unknown waveform, rather than to predict an unknown waveform.

The training and test of the model were conducted by means of 56 FE simulation results described above and three experimental data, respectively. The three test data were boundary conditions similar to the training data as shown in the Design of Experiments (DOE) in Figure B1. The first and second tests, Test 1 and Test 2, respectively, were extracted from the published sled experiments. Test 1 was engaged in the SENIORS project [13], which utilized the test rig consistent with FE simulation. Test 2 was engaged in the University of Virginia [16], which was conducted using Taurus with rear seat equipped with a seatbelt without a load limiter. The third test (Test 3) was conducted at 40 km/h with the test rig processed from a mass-produced small size sedan model. As described in a later section, some of the deflections of ribs without IR-TRACCs were measured in the experiment by means of the optical method.

The loss function for the training of the neural network model was the combination of Mean Squared Error (MSE) and L1 regularization in order to prevent overfitting because of the small size of the training datasets in this study. Moreover, Root MSE (RMSE) and differences of peak resultant deflection, utilized as chest injury criteria such as Rmax and PCscore, were also calculated for the discussion of prediction accuracy, because those dimensioned criteria were more understandable about the amount of the error than that indicated by dimensionless MSE. Smaller values for these error indicators indicated smaller errors. Test 1 and Test 2 were utilized to verify that the DNN model could reconstruct the waveform from the IR-TRACC data as inputs. The loss functions of these two tests were calculated only on the measurable ribs by IR-TRACCs. On the other hand, Test 3 was utilized to verify that the deflection of ribs without IR-TRACCs could be predicted from the time-historical rib deflections of measurable ribs with IR-TRACCs and sled velocities.

Waveform data was preprocessed by standardization, i.e., setting the mean to 0 and the variance to 1. The calculation of the mean and variance for standardization was performed on simulation data alone.

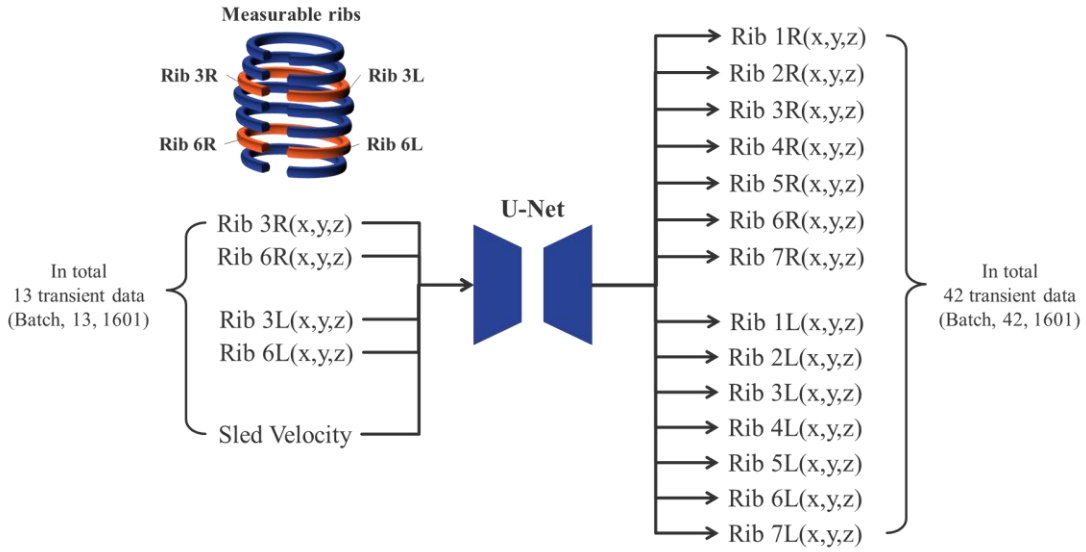

Figure 3. Concept of the model using U-Net

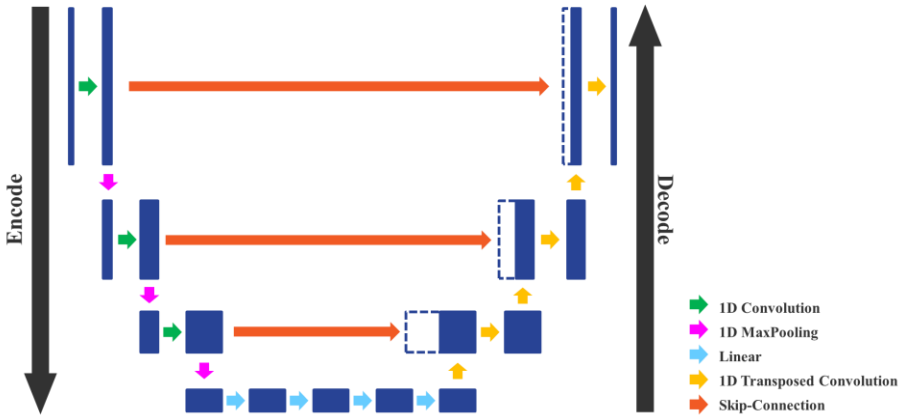

	Layer type	Activation function	BatchNormalization	Dropout ratio	(Channel size, Kernel size, Stride, Padding)	Output size
Encoder	1D Convolution	ReLU	1D BatchNorm	-	(32, 120, 3, 100)	(Batch, 32, 561)
	1D MaxPooling	-	-	-	-	(Batch, 32, 280)※1
	1D Convolution	ReLU	1D BatchNorm	-	(64, 25, 2, 0)	(Batch, 64, 128)
	1D MaxPooling	-	-	-	-	(Batch, 64, 64) ※2
	1D Convolution	ReLU	1D BatchNorm	-	(128, 5, 2, 0)	(Batch, 128, 30)
	1D MaxPooling	-	-	-	-	(Batch, 128, 15) ※3
	Linear	ReLU	1D BatchNorm	-	-	(Batch, 512)
	Linear	Tanh	-	-	-	(Batch, 30)
Decoder	Linear	ReLU	1D BatchNorm	-	-	(Batch, 512)
	Linear	ReLU	1D BatchNorm	-	-	(Batch, 1920)
	Concatenation※3	-	-	-	-	(Batch, 256, 15)
	1D Transposed Convolution	ReLU	1D BatchNorm	-	(128, 4, 2, 1)	(Batch, 128, 30)
	1D Transposed Convolution	ReLU	1D BatchNorm	-	(128, 6, 2, 0)	(Batch, 64, 64)
	Concatenation※2	-	-	-	-	(Batch, 128, 64)
	1D Transposed Convolution	ReLU	1D BatchNorm	0.5	(128, 4, 2, 1)	(Batch, 64, 128)
	1D Transposed Convolution	ReLU	1D BatchNorm	0.5	(128, 26, 2, 0)	(Batch, 64, 280)
	Concatenation※1	-	-	-	-	(Batch, 96, 280)
	1D Transposed Convolution	ReLU	1D BatchNorm	-	(128, 4, 2, 1)	(Batch, 64, 560)
	1D Transposed Convolution	ReLU	1D BatchNorm	-	(128, 124, 3, 0)	(Batch, 42, 1801)
	Cropping	-	-	-	-	(Batch, 42, 1601)

※1, 2, 3 Skip connection

Figure 4. Network architecture diagram and topology of U-Net

Stereoscopic Vision Measurement of the Ribs Without IR-TRACCs

The time-historical deflections of ribs without IR-TRACCs were measured by the stereoscopic vision measurement method in order to test the predicted results. Figure 5 shows the illustration of two sets of the stereo cameras installed on the spine box, which recorded stereoscopic vision for the three-dimensional measurement process. The set of twin cameras was assembled with two high speed cameras (FASTCAM MH6 ST-Cam, Photron, Japan) and its recording frequency was 1000 Hz. The target markers were stuck onto each rib tip. The upper and lower cameras measured the deflections of the 2nd to 3rd ribs and 3rd to 6th ribs, respectively. It was required for the recorded objects and cameras to belong to a common coordinate system. However, the 4th rib on the upper spine box was recorded by lower cameras which were installed on the lower spine box because the upper IR-TRACC was prevented from recording the 4th ribs by the upper cameras. Therefore, the optical measured deflection of the 4th rib was estimated by Equation 1.

$$Estimated\ 4^{th}\ rib\ deflection = 4^{th}\ rib\ deflection \times \frac{Upper\ 3^{rd}\ rib\ deflection}{Lower\ 3^{rd}\ rib\ deflection} \qquad Equation\ (1)$$

The stereoscopic vision measurement was engaged on the left-side ribs alone due to the mounting space limitation of the equipment. The THOR-ATD with the two sets of stereo cameras was installed on the sled test rig representing a small sized sedan and impacted at 40 km/h for data aggregation. The validation accuracy was evaluated by RMSE and differences of peak resultant deflection.

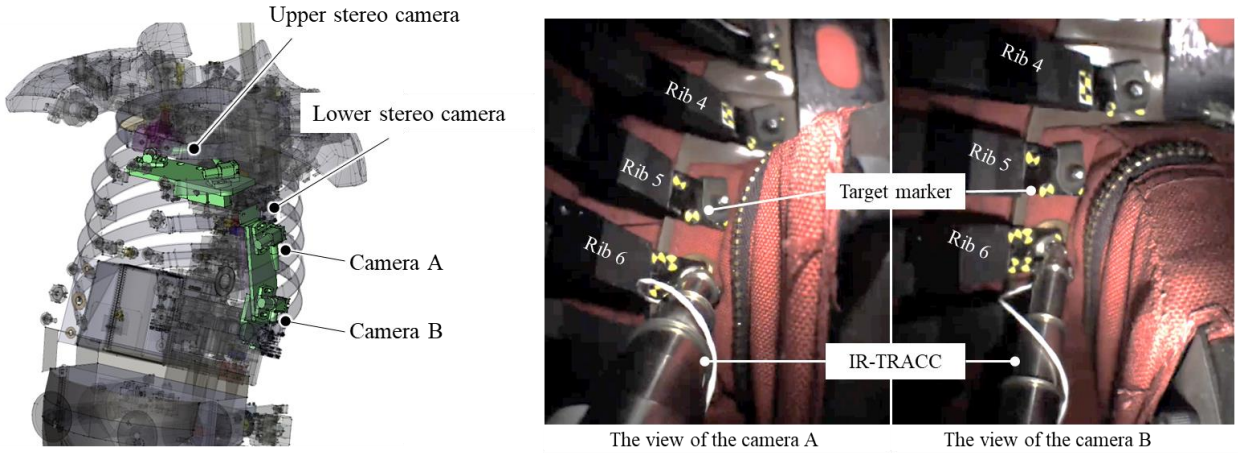

Figure 5. Installation of stereo cameras on the spine box

RESULTS

Learning of the Model

Figure 6 shows the MSE losses of the training and the test and those losses were less than 0.0067 and 0.019, respectively. Figures 7 and 8 show comparisons of the exact and predicted data of Test 1 and Test 2, respectively, and these indicated that the predicted rib deflections overall reconstructed the trend and peaks of exact waveforms. The average RMSE of each test result was less than 1.3 mm. Table 1 shows the RMSE and the differences of the peak resultant deflections of Test 1 and Test 2.

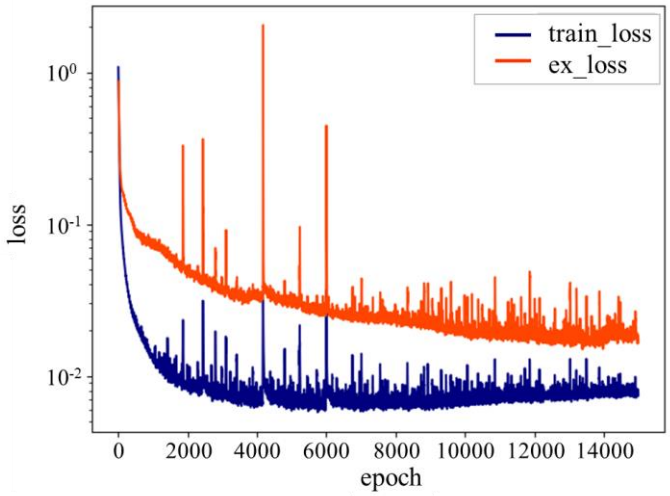

Figure 6. History of MSE loss function

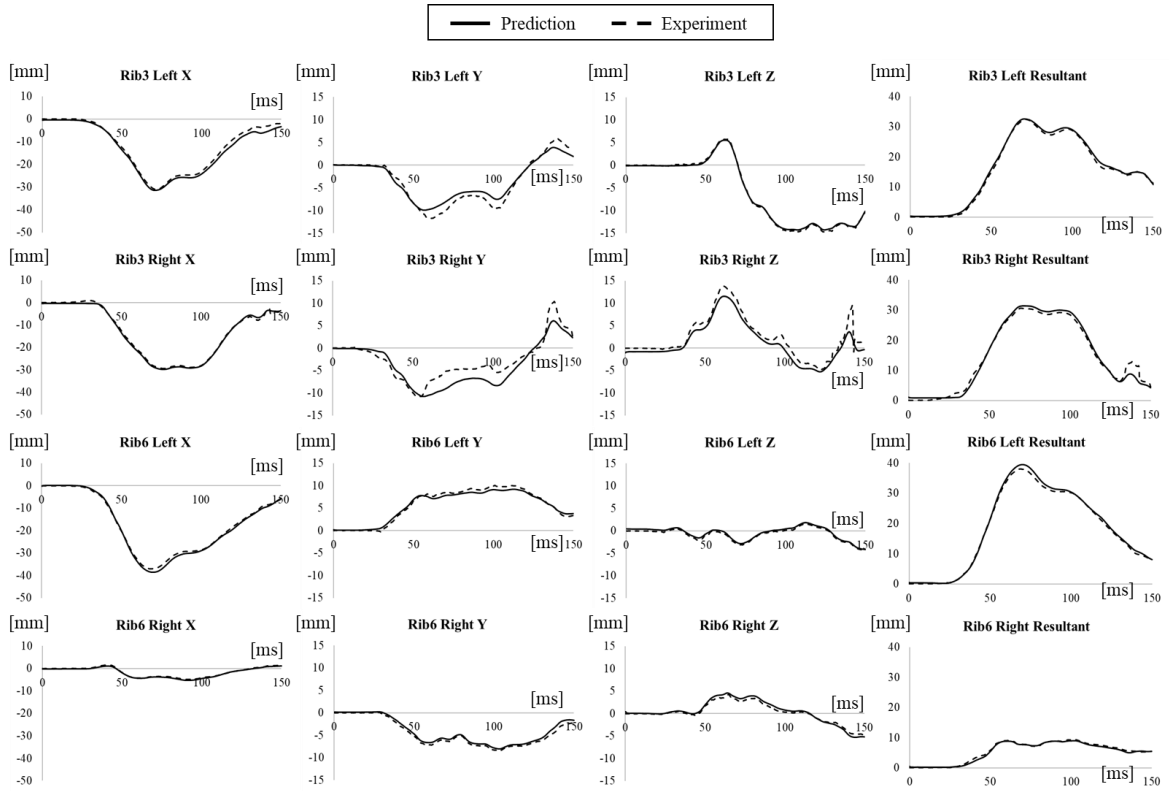

Figure 7. Comparison between predicted and exact rib deflections in Test 1

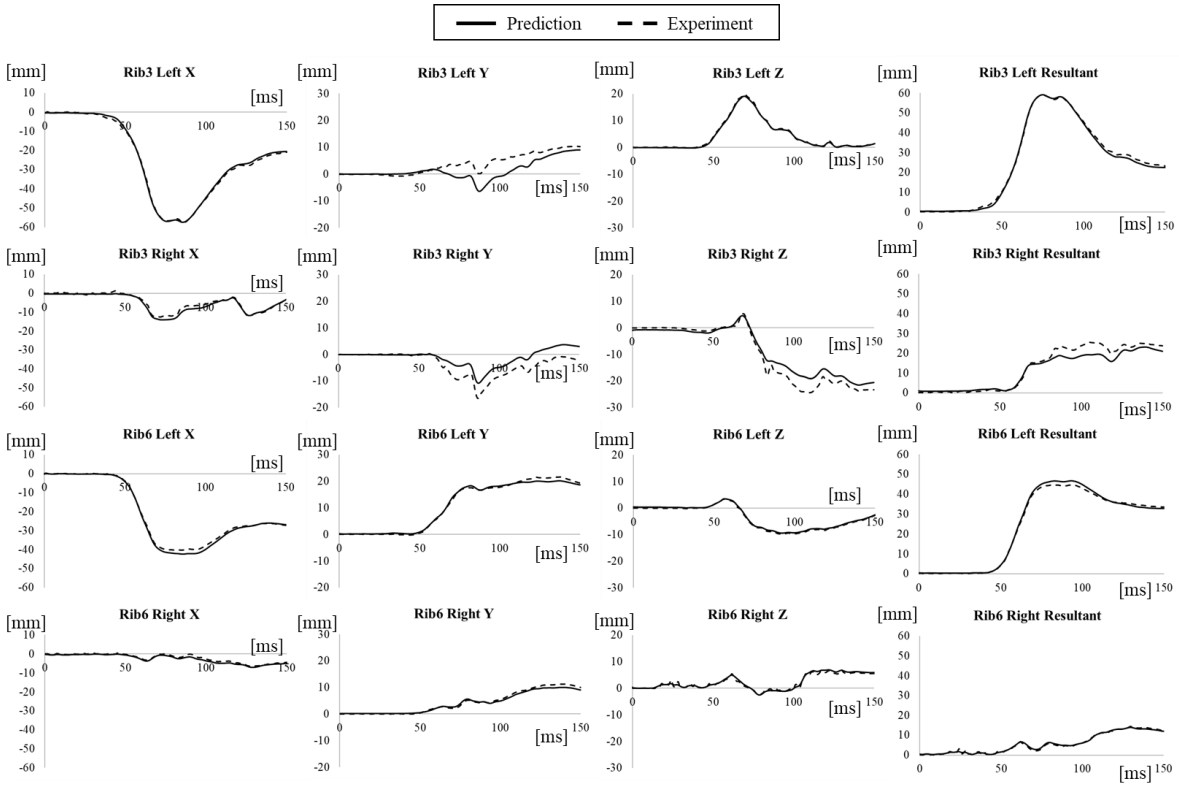

Figure 8. Comparison between predicted and exact rib deflections in Test 2

Table 1.
The RMSE and differences of the peak resultant deflection of Test 1 and Test 2

			X [mm]	Y [mm]	Z [mm]	Resultant [mm]	Differences of Peak Res. between Pred. and Exp. [mm]
Test 1	**Left**	**Rib 3**	1.3	1.1	0.2	1.0	-0.1
		Rib 6	0.8	0.5	0.3	0.7	-1.3
	Right	**Rib 3**	0.6	2.0	1.4	1.3	-0.7
		Rib 6	0.3	0.5	0.4	0.3	0.3
Test 2	**Left**	**Rib 3**	0.7	3.5	0.3	1.0	0.2
		Rib 6	1.0	0.7	0.3	1.0	2.3
	Right	**Rib 3**	0.9	3.2	2.6	2.7	-1.8
		Rib 6	0.6	0.6	0.4	0.4	0.6

The Results of Stereoscopic Vision Measurement

Figure 9 shows a comparison of the deflections measured by IR-TRACCs and stereoscopic vision on the 3rd and 6th ribs, respectively. Table 2 shows the RMSE of the stereoscopic vision measurement compared to the IR-TRACC measurement results. The stereoscopic vision measurement overall traced the rib deflection with small RMSE, particularly, the RMSE of resultant deflection of both the 3rd and 6th ribs were smaller than 1.0 mm.

Figure 10 shows the comparison between the predicted rib deflections through the 2nd to 6th ribs and the optically measured rib deflections. The stereoscopic vision measurement results for the 2nd and 4th ribs were interrupted because of the obstruction of the camera view during the experiment. The noise occurred in the Z direction deflection of the 4th rib because the compensation by the ratio of upper and lower measurement results of 3rd rib deflection rose drastically within a short duration. Table 3 shows the RMSE and the differences of the peak resultant deflections of Test 3.

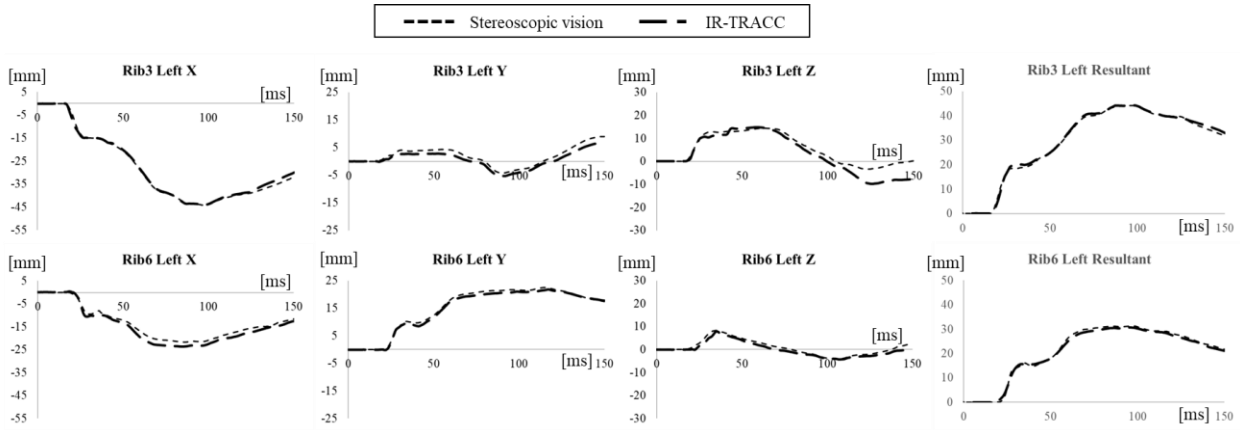

Figure 9. The rib deflection measured by stereoscopic vision compared to that measured by IR-TRACC

Table 2.
The RMSE of the comparison of the stereoscopic vision to the IR-TRACC measurement

		X [mm]	Y [mm]	Z [mm]	Resultant [mm]
Left	**Rib 3**	0.8	1.4	3.5	0.7
	Rib 6	1.7	0.7	1.0	0.8

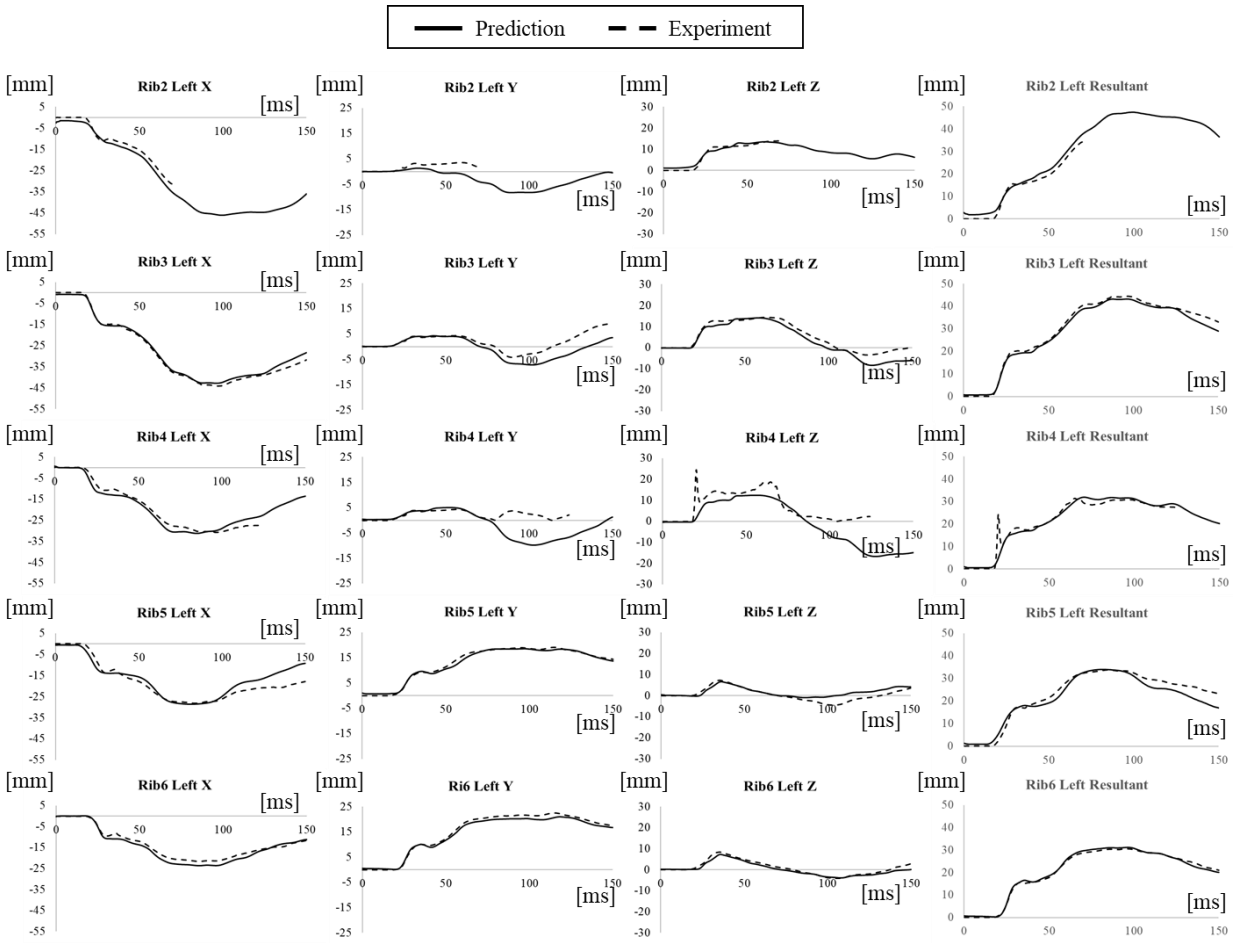

Figure 10. Comparison of predicted deflection by the DNN model and stereoscopic vision

Table 3.
The RMSE and the differences of the peak resultant deflections of Test 3

			X [mm]	Y [mm]	Z [mm]	Resultant [mm]	Differences of Peak Res. between Pred. and Exp. [mm]
		Rib 2	2.3	2.8	1.0	2.1	—
		Rib 3	1.4	3.5	2.8	1.5	1.0
Test 3	**Left**	**Rib 4**	2.1	6.1	6.9	2.3	0.0
		Rib 5	3.6	0.6	2.0	2.7	-0.3
		Rib 6	1.6	1.1	0.9	0.7	-0.6

DISCUSSION

The predicted time-historical rib deflections by DNN model showed errors with smaller RMSE than average 1.5 mm, validated by means of measured deflections by IR-TRACC and stereoscopic vision. Table 3 showed that the differences of predicted and experimental peak resultant deflection in Test 3 indicated smaller error than ±1.0 mm also in ribs without IR-TRACCs, although the model was trained by a small number of datasets. The reason for such small errors was assumed to be that the FE model for the training data was validated sufficiently to represent the actual mechanical properties among the ribs with and without IR-TRACCs and that information was included in the DOE of the 56 training simulation results. In addition, the THOR-ATD bib was independently validated under three-

point bending loading conditions [17]. Owing to these validations, the mechanical property of the FE simulation was assumed to represent the actual properties with high accuracy, resulting in the decrease of DNN prediction error.

Although resultant deflections were predicted with small errors, Y direction deflection in the upper ribs showed larger errors than those of X and Z direction deflections. These trends were indicated consistently within the test results of Tests 1, 2, and 3. This was considered to be due to the influence of some of the boundary conditions of the thoracic calibration test for THOR-ATD, even though the THOR-ATD FE model overall represented well the experimental results with high accuracy. The thoracic calibration was conducted by horizontally impacting the probe on the thorax of THOR-ATD vertically seated on the test table. The response curve of force and deflection was confirmed to fall into the corridor [17]. As shown in Figure 1, since the tips of the ribs on the THOR-ATD are downward in order to more exactly represent human ribs, the directions of deflection of the impacted ribs are dominantly the X and Z directions. Consequently, Y direction deflection was relatively smaller than those of the other two directions. Hence, the validation of Y deflection would be insufficient by the calibration test, whereas the validation accuracy of X and Z deflection was improved by fitting within the response curve corridor. Furthermore, the amount of Y deflection was smaller than those of the other two directions, resulting in increasing the sensitivity against the error, which might decrease the validation accuracy. On the other hand, the oblique impact calibration test was conducted on the lower part of the thorax. The test mode may improve the accuracy of Y direction deflection of the ribs in the lower part.

The RMSE of the right 3rd rib deflection was more than twice those of the three predictions. Those results may be due to the influence of the seat belt path, which passes from the right shoulder to the left abdomen as shown in Figure 11. The seat belt passes on the surface of left 3rd rib and directly push into the thorax. On the other hand, seat belt force on the right thorax was transmitted to the 3rd rib indirectly through the 1st and 2nd ribs. Maatouki et al. reported that the validation accuracy of the 3rd rib deflection was small when the probe impacted on an upper surface of the thorax around the 1st and 2nd ribs compared to when impacting directly on the 3rd rib [17]. Furthermore, although the THOR-ATD FE model was validated by the sled experiment using a seat belt, the main focus of the test was on the deflection of the ribs right under the seatbelt path where the maximum rib deflection mainly occurred. Therefore, the priority of the validation accuracy improvement was low on the ribs far from the seatbelt. For these reasons, the validation accuracy of the right 3rd rib was inferior to the other three ribs with IR-TRACCs and the prediction accuracy was also smaller than those of the other three ribs. Whereas the right 6th rib was also far from seat belt path, the influence of the seatbelt path may be small because the amount of the deflection itself was small.

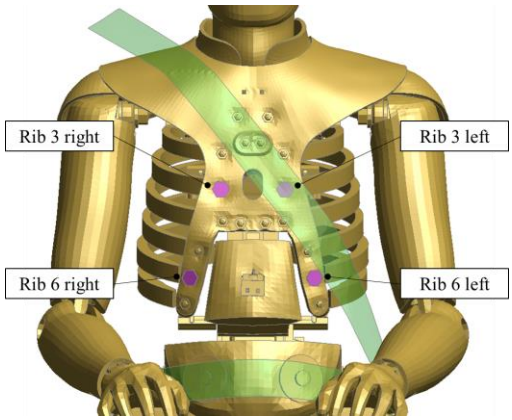

Figure 11. Illustration showing the location of seat belt path and IR-TRACC

As limitations, the prediction accuracy of a specific direction was small due to the influence of the validation test condition and the seat belt path. Some of the ribs indicated an RMSE smaller than 1.0 mm. However, it would be necessary to improve the accuracy in order to replace a physical measurement device used for the assessment test. The additional learning data under various boundary conditions would be necessary in order to improve the prediction accuracy. Furthermore, this study validated only the 2nd to 6th ribs on the left side, and the other ribs also need to be validated.

CONCLUSIONS

The DNN model constructed by the FE simulation predicted all time-historical rib deflections from the four IR-TRACCs and the sled velocity as input data. When the well-validated FE simulation results were used as training data, the DNN was able to learn the physical characteristics, which could predict the time-historical deflection of the physical THOR-ATD. These results indicated the potential for application of the artificial intelligence model as an alternative to the measurement devices.

REFERENCES

[1] Kent, R.W., Henary, B., Matsuoka, F., 2005. "On the fatal crash experience of older drivers." Annu Proc Assoc Adv Automot Med. 49: 371–391.

[2] Kent, R.W., Woods, W., Bostrom, O., 2008. "Fatality risk and the presence of rib fractures." Ann Adv Automot Med. 52: 73–84.

[3] National Highway Traffic Safety Administration. 2017. "Traffic Safety Facts 2015." DOT HS 812 372, 1-5, Available at https://crashstats.nhtsa.dot.gov/#/DocumentTypeList/12. Accessed November 23, 2022

[4] Stawicki, S. P., Grossman M. D., et al., 2004. "Rib Fractures in the Elderly: A Marker of Injury Severity." Journal of the American Geriatrics Society. 52(5): 805-808.

[5] Bergeron, E., Lavoie, A., et al., 2003. "Elderly trauma patients with rib fractures are at greater risk of death and pneumonia." The Journal of Trauma: Injury, Infection, and Critical Care, 54(3): 478-485

[6] Bulger, E. M., Arneson, M. A., Mock, C. N. Jurkovich, G. J., 2000. "Rib Fractures in the Elderly." The Journal of Trauma: Injury, Infection, and Critical Care, 48(6): 1040-1047

[7] Kent, R.W., Patrie, J., Poteau, F., 2003. "Development of an age-dependent thoracic injury criterion for frontal impact restrain loading." The Proceedings of 18th International Technical Conference on Enhanced Safety of Vehicles (ESV), Nagoya, Japan; 12

[8] Craig, M., Parent, D., Lee, E., Rudd, R., Takhounts, E., Hasija, V., 2020. "Injury Criteria for the THOR 50th Male ATD.", Available at https://lindseyresearch.com/wp-content/uploads/2021/10/NHTSA-2020-0032-0005-Injury-Criteria-for-the-THOR-50th-Male-ATD.pdf. Accessed November 23, 2022

[9] Poplin, G.S., McMurry, T.L., Forman, J. L., Ash, J., Parent, D. P., Craig, M. J., Song, E., Kent, R., Shaw, G., Crandall, J., 2017. "Development of thoracic injury risk functions for the THOR ATD.", Accident Analysis and Prevention, 106: 122-130

[10] Kawabuchi, T., Yasuhiro, D., 2019. "Evaluation of Thoracic Deflection Criteria in Frontal Collision Using Thoracic Impactor Simulation with Human Body FE Model.", The Proceedings of 26th International Technical Conference on Enhanced Safety of Vehicles (ESV), Einthoven, Netherland

[11] Guo, X., Li, W., Lorio, F., 2016., "Convolutional Neural Networks for Steady Flow Approximation.", The Proceedings of 22nd ACM SIGKDD International Conference on Knowledge Discovery and Data Mining: 481-490

[12] Ito, O., Shiraishi, J., "A Study of Pedestrian Head Protection CAE Accuracy Improvement Using Deep Learning (Japanese)", Paper presented at: Society of Automotive Engineers of Japan (JSAE), paper #20206294

[13] European Commission Eighth Framework Programme Horizon 2020, 2017. "Safety Enhanced Innovations for Older Road Users", Deliverable 2.5a

[14] Humanetics Innovative Solutions, 2016. "THOR-50th Metric V1.3.2 LS-DYNA Model Technical Report User's Manual."

[15] Ronneberger, O., Fischer, P., Brox, T., 2015. „U-Net: Convolutional Networks for Biomedical Image Segmentation.", ArXiv 1505.04597

[16] Crandall, J., 2013. "Thor Metric SD3 Shoulder Advanced Frontal Crash Test Dummy.", DTNH22-09-H-00247

[17] Maatouki, I., Fu, S., Zhou, Z., 2018. „Latest FE Model Development of THOR-50M Crash Test Dummy", 15th International LS-DYNA Users Conference

Appendix A
Table A1.
The load case of the training and test data

Test No.	Peak impact velocity [km/h]	Impact angle [deg]	Load limiter	D-Ring position	Airbag	Seat type
1	25	0	No	D1	No	Steel pan
2	25	0	Low	D2	No	Steel pan
3	25	30	Med	D3	Yes	Steel pan
4	35	0	No	D2	No	Steel pan
5	35	0	Low	D3	Yes	Steel pan
6	35	30	Med	D1	No	Steel pan
7	45	0	Med	D2	No	Steel pan
8	45	30	No	D3	No	Steel pan
9	25	0	Med	D3	No	Steel pan
10	25	0	No	D1	Yes	Steel pan
11	25	30	Low	D2	No	Steel pan
12	35	0	Low	D3	No	Steel pan
13	35	0	Med	D1	No	Steel pan
14	35	30	No	D2	Yes	Steel pan
15	45	0	Med	D2	Yes	Steel pan
16	45	0	No	D3	No	Steel pan
17	45	30	Low	D1	No	Steel pan
18	45	0	Super	D2	No	Steel pan
19	40	0	Super	D2	No	Steel pan
20	50	0	High	D2	No	Steel pan
21	45	0	High	D2	No	Steel pan
22	40	30	No	D1	No	Steel pan
23	40	30	Super	D2	No	Steel pan
24	40	30	High	D3	No	Steel pan
25	45	30	Super	D3	No	Steel pan
26	45	30	High	D1	No	Steel pan
27	45	30	No	D2	No	Steel pan
28	50	30	No	D3	No	Steel pan
29	50	30	Super	D1	No	Steel pan

Test No.	Peak impact velocity [km/h]	Impact angle [deg]	Load limiter	D-Ring position	Airbag	Seat type
30	56	0	No	D1	Yes	Steel pan
31	56	0	Med	D1	No	Steel pan
32	56	0	Super	D1	No	Steel pan
33	45	30	No	D1	No	Steel pan
34	45	30	Super	D1	Yes	Steel pan
35	45	30	Med	D1	Yes	Steel pan
36	64	15	Super	D1	No	Steel pan
37	64	15	No	D1	Yes	Steel pan
38	64	15	Med	D1	Yes	Steel pan
39	56	0	Med	D1	No	Steel pan
40	56	0	Super	D1	No	Steel pan
41	56	0	No	D1	Yes	Steel pan
42	64	15	Super	D1	Yes	Steel pan
43	64	15	No	D1	No	Steel pan
44	64	15	Med	D1	Yes	Steel pan
45	56	0	Med	D1	No	Steel pan
46	56	0	Super	D1	No	Steel pan
47	56	0	No	D1	Yes	Steel pan
48	64	15	Super	D1	Yes	Steel pan
49	64	15	No	D1	No	Steel pan
50	64	15	Med	D1	Yes	Steel pan
51	55	0	No	D1	No	Steel pan
52	55	0	No	D1	Yes	Steel pan
53	55	0	Med	D1	Yes	Steel pan
54	55	0	Super	D1	No	Steel pan
55	55	0	Super	D1	Yes	Steel pan
56	55	0	Med	D1	No	Steel pan
Test 1	35	0	Low	D3	Yes	Steel pan
Test 2	48	0	No	Others	No	Cushion
Test 3	40	0	Med	Others	No	Cushion

Appendix B

Figure B1.

Visualized diagram of DOE